International Journal of Thermal Sciences 48 (2009) 1786–1799

Contents lists available at ScienceDirect

International Journal of Thermal Sciences

journal homepage: www.elsevier.com/locate/ijts

Simulating low temperature diesel combustion with improved spray models

Shijin Shuai [a], Neerav Abani [b], Takeshi Yoshikawa [b], Rolf D. Reitz [b,*], Sung Wook Park [c]

[a] *State Key Laboratory of Automotive Safety and Energy, Tsinghua University, Beijing, 100084, China*
[b] *Engine Research Center, 1500 Engineering Drive, University of Wisconsin-Madison, Madison, WI 53706, USA*
[c] *Department of Mechanical Engineering, Hanyang University, Seoul 133-791, Republic of Korea*

ARTICLE INFO

Article history:
Received 11 July 2008
Received in revised form
21 January 2009
Accepted 21 January 2009
Available online 14 March 2009

Keywords:
Low temperature combustion
Spray modeling
Gas-jet theory
Droplet collision
CFD

ABSTRACT

Current spray models based on the Lagrangian-droplet and Eulerian-fluid (LDEF) method in the KIVA-3V code are strongly mesh dependent due to errors in predicting the droplet–gas relative velocity and errors in describing droplet–droplet collision and coalescence processes. To reduce the mesh dependence, gas-jet theory is introduced to predict the droplet–gas relative velocity, and a radius of influence (ROI) of collision methodology is established for each gas phase cell to estimate the collision probability for each parcel in the cell. Spray and combustion processes in a low temperature combustion diesel engine under early and late injection strategies with a fine mesh were predicted using the conventional LDEF model and compared with the measurements of soot, OH, fuel liquid and vapor distributions obtained by laser based diagnostics including, PLIF, LII, and Mie scattering. Then, the KIVA-3V code implemented with the improved spray model based on the gas-jet model and modifications of the spray models was utilized to simulate the processes on a relatively coarse numerical mesh. Comparison of the simulations between the fine and coarse meshes shows that the improved spray model can greatly reduce the mesh dependence for low temperature combustion diesel engine CFD simulations.

1. Introduction

Currently spray models based on the LDEF approach are widely used by both the engine and spray industries. Spray models based on a complete Eulerian approach for both the liquid and gas phases have also been of interest. However, both of these approaches have limitations when using coarse numerical meshes in predicting the spray structure, penetration and drop sizes, as shown by Abani et al. [1] for LDEF-based models, and by Abraham [2] for the Eulerian approach. Coarse meshes are desired in order to reduce computer times for detailed multi-dimensional spray simulations. In both methods, adequate resolution of the flow near the nozzle is required down to sizes the order of the injector-hole size for better spray predictions. In addition, it was shown by Abani et al. [1] that even with an adequate resolution, the drop sizes are predicted poorly due to the failure of standard collision models, which are based on O'Rourke and Bracco's collision approach [3] that uses the cell volume as the collision volume. These models over-predict the penetration of sprays. They found that the collision model and the two-way momentum coupling of the two phases can be corrected separately to get an accurate mesh-independent spray prediction in terms of spray structure, penetration and droplet sizes. In their analysis, the error in the droplet–gas relative velocity increases as the mesh becomes coarser and the error in droplet–droplet collision predictions increases as the mesh becomes finer.

Other previous studies regarding the grid dependency of spray models include the near-field study of gas-jets and sprays by Post et al. [4]. They found that none of the available Lagrangian-droplet models gave resolution-independent results when the spatial distribution of the droplets is highly non-uniform. This investigation of the near-nozzle region of sprays was thus inconclusive regarding the entrainment characteristics of the gas in the near-field. Aneja and Abraham [5] compared the liquid penetration obtained from computations with that of experiments and concluded that the predicted liquid penetration in vaporizing sprays is sensitive to the grid resolution and to the details of the collision model [5,6].

Beard et al. [6] and Abani et al. [1] both found that the source of grid dependency is due to inaccurate two-way momentum coupling when the droplet–gas relative velocity is inaccurately predicted. Beard et al. [6] considered an expanding cloud of influence of momentum surrounding droplet parcels and interpolated the droplet velocity and the CFD cell velocity at the cloud interface to obtain an effective gas velocity. This provided a better estimate of

---

[*] Corresponding author. Tel.: +1 608 262 0145; fax: +1 608 262 6707.
E-mail address: reitz@engr.wisc.edu (R.D. Reitz).

1290-0729/$ – see front matter © 2009 Published by Elsevier Masson SAS.
doi:10.1016/j.ijthermalsci.2009.01.011

Nomenclature

AHRR	apparent heat release rate
ATDC	after top dead center
BB-PLIF	broadband planar laser induced fluorescence
BDC	bottom dead center
CAD	crank angle degree
CCD	charge coupled device
CF	cool flame
CFD	computational fluid dynamics
DI	direct injection
HCCI	homogeneous charge compression ignition
ID	ignition delay
IVC	intake valve close
KH	Kelvin–Helmholtz
LDEF	Lagrangian-droplet and Eulerian-fluid
LII	laser induced incandescence
LL	liquid–fuel penetration or liquid length
LMS	laser Mie scattering
MK	modulated kinetics
NTC	no-time counter
PAHs	polycyclic aromatic hydrocarbons
PLIF	planar laser induced fluorescence
RNG	renormalization group
ROI	radius of influence
RT	Rayleigh–Taylor
SMD	Sauter mean diameter
SSC	second stage combustion
UV	ultraviolet

droplet–gas relative velocity as compared to conventional LDEF spray models. On the other hand Abani et al. [1] suggested to predict the droplet–gas relative velocity using turbulent gas-jet theory. This avoided the need for the interpolation required in Beard's model and also provides accurate spray-tip penetration and structure predictions.

Inter-droplet collisions and especially the resultant coalescence and fragmentation processes are central to determining droplet distributions and mixing processes in non-dilute spray systems. Modeling of collisions involves two distinct problems: the numerical problem of predicting the probability of a collision and the physical problem of predicting the effect of the collision, viz., the type of outcome and the post-collision characteristics. The major challenge in collision probability predictions is preserving accuracy in the calculations without undesirable numerical dependencies, such as sensitivity of the results to the gas phase mesh size and/or the computational time-step. Currently, one of the most widely used collision models is the O'Rourke collision model [3], which has investigated by various researchers. Schmidt and Rutland [7,8] improved the O'Rourke and Bracco collision model by using a separate collision mesh, and further sampled potential collision partners so as to speed-up the collision computations using the "no-time counter" (NTC) approach. They found that due to the non-uniform spatial distribution of spray droplets, the collision frequency is different on different grids. This affects the predicted Sauter mean diameter (SMD) of the spray droplets and hence, different grids result in different vaporization and liquid penetration predictions. Lippert et al. [9] also used a similar idea of a separate collision mesh, along with an adaptive mesh which resolved the near-nozzle region finely enough to predict accurate spray structures. However, the use of extra cells near the nozzle also increases computation times.

Several LDEF-based spray models employ an atomization model that considers breakup to be due to Kelvin–Helmholtz and Rayleigh–Taylor (KH–RT breakup) instabilities [10]. Abani et al. [1] demonstrated grid-independency in spray calculations for injections into a constant volume chamber under steady injection conditions. In their model it was proposed that the air entrainment into the jet can be modeled according to gas-jet theory [11,12]. A sub-grid scale model was introduced whereby the axial component of the droplet–gas relative velocity is corrected using the assumption that the relative velocity is that between the liquid droplets and a corresponding equal momentum gas-jet. In a further study Abani et al. [13] applied the improved model to simulate conventional diesel engine combustion and showed that it reduced grid dependency in terms of the predicted pressure trace, heat release rate and fuel–vapor distribution inside the combustion chamber under different engine conditions. To improve the droplet–gas relative velocity prediction in the case of time-varying injection conditions, they used Duhamel's superposition integral in conjunction with a response function and eddy response time, consistent with the Helmholtz Vortex theory [14]. For consistency in the droplet size predictions they used a collision model based on a radius of influence (ROI) approach, as suggested by Abani et al. [1] and Munnannuar et al. [15,16], with outcomes of grazing and coalescence collisions only, as proposed by O'Rourke and Bracco [3].

In the ROI collision model, potential collision partners for a given droplet are considered within a collisional volume of a specified radius around it, as opposed using the CFD mesh cell as the collisional volume, as in the standard collision model. Later Munnannur and Reitz [15,16] also incorporated more collision outcomes, including bounce, fragmenting and non-fragmenting drop separation, as well as regrouping of droplet parcels in order to prevent the generation of a large number of drop parcels. These spray models have also been shown to reduce time-step dependency [1].

In the present paper, the gas-jet and radius of influence (ROI) collision models suggested by Abani et al. [1] were implemented into the KIVA-3V code [17] to simulate spray processes for low temperature diesel combustion with early and late injection strategies. Two different mesh sizes were considered and comparisons were made of predicted soot, OH, fuel liquid and vapor distributions with measurements made by PLIF, LII and Mie scattering [18]. The results from the computations with the improved spray models were found to agree well with the measurements and are also shown to reduce numerical grid dependency effects.

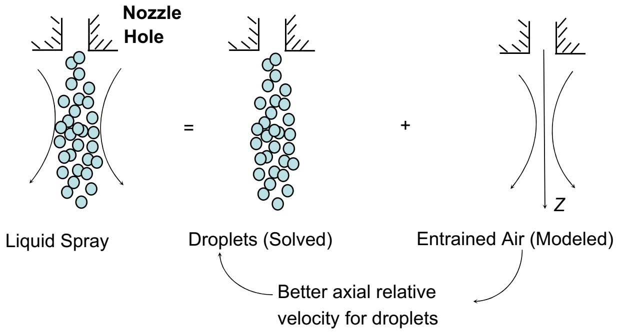

Fig. 1. Schematic of gas-jet-based diesel spray model.

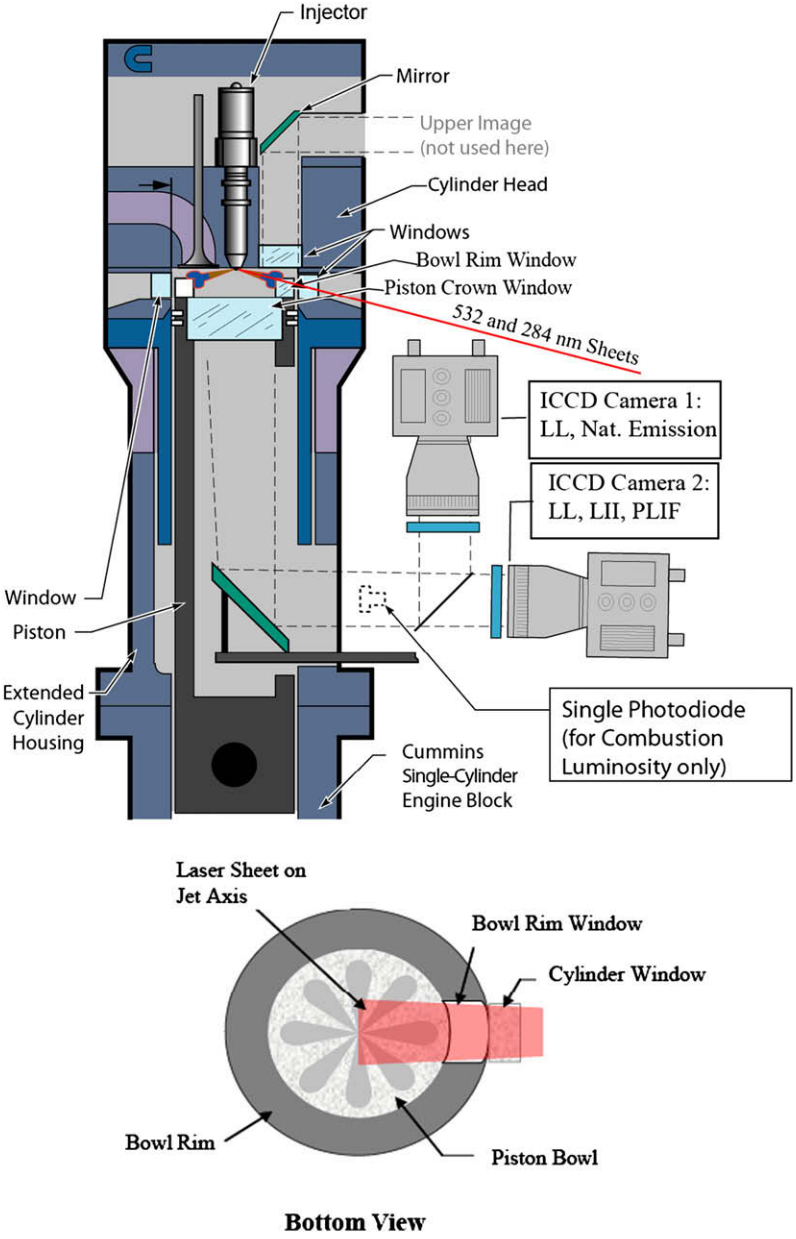

Fig. 2. Sandia/Cummins engine, laser sheet and camera setup orientations [18].

2. Spray and combustion models

2.1. Gas-jet model

The basic idea of the present model is depicted in Fig. 1. A spray flow has two components: the group of droplets which forms the liquid phase, and the air entrained which forms the gas phase. For reducing grid dependency the motion of either of the phases could be corrected since they are coupled by their respective transport equations.

The LDEF stochastic spray model considers a group of identical droplets known as a parcel, which is tracked in a Lagrangian approach. The gas phase is modeled using an Eulerian approach. The conservation equation for a parcel is represented by the conservation equation of a single droplet in that parcel. In the present model, the axial component of the gas phase velocity in the droplet equations is modeled using gas-jet theory in the region near the nozzle exit. The droplet momentum equation is given as

$$\frac{\mathrm{d}U}{\mathrm{d}t} = \frac{3}{8} C_{\mathrm{D}} \frac{\rho_{\mathrm{g}}}{\rho_{\mathrm{l}}} \frac{1}{D} \left| U - V_{\mathrm{gas}} \right| \left(U - V_{\mathrm{gas}} \right) \tag{1}$$

where U is the droplet velocity vector, D is the droplet diameter and V_{gas} is the surrounding gas phase velocity vector. The drag coefficient, C_{D} is assumed to be a function of droplet Reynolds number [17]. The surrounding gas phase velocity vector is given as $V_{\mathrm{gas}} = (V_x, V_y, V_z)$, where V_y and V_z are the perpendicular components of the surrounding gas phase velocity obtained from the CFD solution, and the axial component (considered as the x-direction here) is given by gas-jet theory as [9,19]

$$V_x = V_{\mathrm{gas}} = \min \left[U_{\mathrm{inj}}, \frac{3 U_{\mathrm{inj}}^2 d_{\mathrm{eq}}^2}{\left[32 \nu_{\mathrm{t}} x \left(1 + \frac{3 U_{\mathrm{inj}}^2 d_{\mathrm{eq}}^2 r^2}{256 \nu_{\mathrm{t}}^2 x^2} \right)^2 \right]} \right] \tag{2}$$

Table 1
Sandia/Cummins engine and injector specifications [18].

Engine base type	Cummins N-14, DI diesel
Number of cylinders	1
Number of intake valves	2
Number of exhaust valves	1[a]
Combustion chamber	Quiescent, direct injection
Swirl ratio	0.5
Bore × stroke, cm	13.97 × 15.24
Bowl width, depth, cm	9.78, 1.55
Displacement, L	2.34
Connecting rod length, cm	30.48
Geometric compression ratio	11.2:1
Simulated compression ratio[b]	16:1
Fuel injector type	Common rail, pilot valve actuated
Cup (tip) type	Mini sac
Number of holes	8, equally spaced
Spray pattern included angle	152°
Rail pressure, bar	1600
Nozzle orifice diameter, mm	0.196
Nozzle orifice L/D	5

[a] In this optically accessible diesel engine, one of the two exhaust valves of the production cylinder head was replaced by a window and periscope.

[b] TDC conditions for a 16:1 compression ratio engine are produced in the optical engine by preheating and boosting the intake stream.

Here U_{inj} is the injection velocity of the liquid-jet which is also assumed to be the injection velocity of the gas-jet. x is the axial distance of the droplet parcel from the injector tip and r is the radial distance of the parcel from the spray axis. Thus, the relative velocity between the droplets and the gas phase in the potential core near-nozzle region is assumed to be zero. d_{eq} is the equivalent diameter of the gas-jet defined as [11]

$$d_{\mathrm{eq}} = d_{\mathrm{noz}}\sqrt{\frac{\rho_{\mathrm{l}}}{\rho_{\mathrm{g}}}} \tag{3}$$

where d_{noz} is the effective nozzle diameter, and ρ_{l} and ρ_{g} are the liquid and gas phase densities, respectively. ν_{t} is the turbulent viscosity for jets given as [11]

$$\nu_{\mathrm{t}} = C_{\mathrm{t}}\pi^{0.5}U_{\mathrm{inj}}d_{\mathrm{eq}}/2, \quad \text{where } C_{\mathrm{t}} = K/\left(16\pi^{0.5}\right) \tag{4}$$

and C_{t} is a constant, as reported by Abraham [11], who used $C_{\mathrm{t}} = 0.0161$. In the present case C_{t} is tuned to 0.0317 by setting the entrainment constant $K = 0.9$ for this diesel low temperature combustion. These constants determine the effective turbulent diffusion of a jet and hence the turbulent mixing rate.

The axial component of the source terms in the drop–gas momentum coupling conservation equations is modeled using the modified relative velocity, as proposed by Abani et al. [13]. Only for the breakup model, the gas phase velocity from the CFD prediction is maintained. This is also justified by the fact that the droplet breakup correlations used in the atomization model are based on far-field information. Thus, the surrounding gas velocity from the CFD mesh is used to represent the external force in the jet breakup process.

2.2. Spray breakup model

In this study the Kelvin–Helmholtz (KH) breakup model was used within the breakup length or intact core region near the nozzle exit. The Rayleigh–Taylor (RT) model is then used in conjunction with the KH model to predict the secondary breakup of droplets beyond the intact core region. The breakup constants used in the KH–RT breakup model, as proposed by Beale and Reitz [10] were tuned for the new spray model. The KH model postulates that a parent parcel with radius r breaks up to form new drops of radius r_{c}, such that:

$$r_{\mathrm{c}} = B_0\Lambda_{\mathrm{KH}} \tag{5}$$

where Λ_{KH} is the wavelength corresponding to a KH wave with maximum growth rate Ω_{KH}, and B_0 is a constant equal to 0.61 in the standard model. The frequency of the fastest-growing wave and its corresponding wavelength is given by [10]

$$\Omega_{\mathrm{KH}} = \frac{0.34 + 0.38We_{\mathrm{g}}^{1.5}}{(1+Z)\left(1+1.4T^{0.6}\right)}\sqrt{\frac{\sigma}{\rho_{\mathrm{l}}r^3}} \tag{6}$$

$$\Lambda_{\mathrm{KH}} = \frac{9.02r\left(1+0.45\sqrt{Z}\right)\left(1+0.4T^{0.7}\right)}{\left(1+0.865We_{\mathrm{g}}^{1.67}\right)^{0.6}} \tag{7}$$

where We_{g} is the gas Weber number, Z is the Ohnesorge number and T is the Taylor number defined as

$$We_{\mathrm{g}} = \frac{\rho_{\mathrm{g}}U_{\mathrm{r}}^2 r}{\sigma}; \quad Z = \frac{\sqrt{We_{\mathrm{l}}}}{Re_{\mathrm{l}}}; \quad T = Z\sqrt{We_{\mathrm{g}}} \tag{8}$$

where U_{r} is the drop–gas relative velocity, and We_{l} is the liquid Weber number based on liquid fuel density ρ_{l}. During breakup, the parent drop reduces in diameter due to mass loss associated with the shed droplets. The rate of change of radius of the parent drop, $\mathrm{d}r/\mathrm{d}t$ is evaluated considering the breakup time τ_{KH} as

$$\frac{\mathrm{d}r}{\mathrm{d}t} = -\frac{r - r_{\mathrm{c}}}{\tau_{\mathrm{KH}}}; \quad \tau_{\mathrm{KH}} = \frac{3.726B_1 r}{\Omega_{\mathrm{KH}}\Lambda_{\mathrm{KH}}} \tag{9}$$

where the standard model uses B_1 equal to 40 [10].

The RT model is also based on wave instability considerations and the droplet deceleration in the spray is the main driving force of breakup with the frequency of the fastest-growing wave given as [10]

$$\Omega_{\mathrm{RT}} = \sqrt{\frac{2}{3\sqrt{3\sigma}}\frac{\left[-a_{\mathrm{t}}\left(\rho_{\mathrm{l}}-\rho_{\mathrm{g}}\right)\right]^{3/2}}{\rho_{\mathrm{l}}+\rho_{\mathrm{g}}}} \tag{10}$$

where a_{t} is the drop acceleration in the direction of travel. The corresponding wave number is given as

Table 2
Fuel specifications [18].

Total aromatics by volume	27%
Olefins	0.5%
Saturates	72.5%
Sulfur (by weight)	9.1 ppm
Distillation temperatures	
Initial boiling point	190 °C
10% Distillation temperature	212 °C
50% Distillation temperature	254 °C
90% Distillation temperature	315 °C
End point	350 °C
Cetane number	46
Specific gravity at 20 °C	0.8426
C/H by weight	6.5
Net heat of combustion	43 MJ/kg
Viscosity at 40 °C	2.35 cS

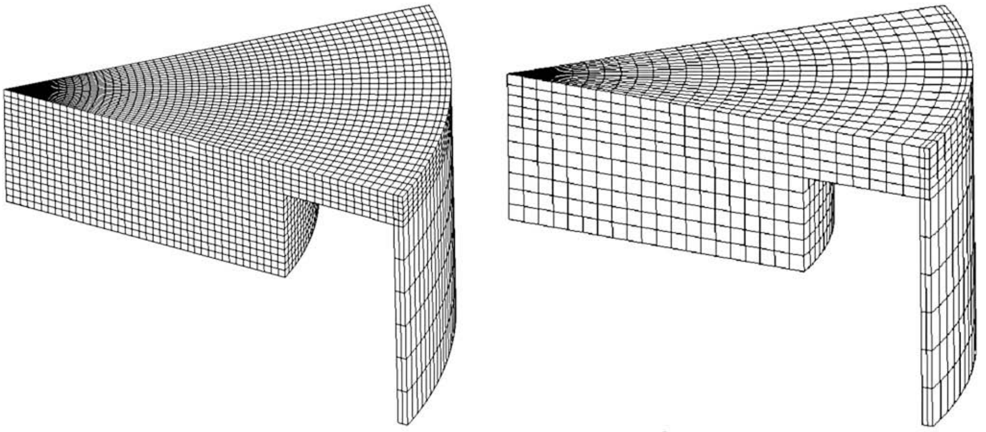

Fig. 3. Fine and coarse computational grids shown at TDC.

$$K_{\mathrm{RT}} = \sqrt{\frac{-a_{\mathrm{t}}\left(\rho_{\mathrm{l}} - \rho_{\mathrm{g}}\right)}{3\sigma}} \tag{11}$$

The wavelength corresponding to the fastest wave growth rate is $2\pi C_{\mathrm{RT}}/K_{\mathrm{RT}}$ and is compared to the droplet radius to decide the breakup drop sizes. The wave growth is tracked with time and is compared to the breakup time, defined as

$$\tau_{\mathrm{RT}} = \frac{C_\tau}{\Omega_{\mathrm{RT}}} \tag{12}$$

where C_τ is a constant equal to 1.0 for the standard model. If RT waves grow for a time greater than or equal to the breakup time, the drop is assumed to breakup. The radii of the new child drops are evaluated as

$$r_{\mathrm{c}} = \frac{\pi C_{\mathrm{RT}}}{K_{\mathrm{RT}}} \tag{13}$$

where C_{RT} is an adjustable constant set equal to 0.1 in the standard model.

The KH and RT breakup sub models use the CFD cell value velocities as the gas phase velocity to evaluate the drop acceleration and relative velocities. However, with the new spray model, the droplet velocities are more accurately predicted by using the gas-jet velocity estimate for the droplet drag evaluation. It was found that the gas-jet model reduced the grid dependency of the spray. However, the use of the standard model constants under-predicted the spray-tip penetration and produced larger droplet sizes, resulting in slower evaporation in low temperature diesel combustion. This was found to be especially true for the RT breakup mechanism as the droplet acceleration is sensitive to droplet drag-forces. In order to control the breakup to avoid slower evaporation, the RT breakup constants were modified to get faster breakup and smaller child droplet sizes. The constant C_τ was set to 0.5 and C_{RT} was set to 0.05 based on the comparisons to experimental pressure history. In addition, the constants B_0 and B_1 in the KH model were increased to 4.5 and 60 respectively to achieve a longer liquid penetration at the beginning of spray, consistent with the suggestions of Abani et al. [1].

Table 3
Low temperature injection strategies [18].

	Early injection	Late injection
Speed (rpm)	1200	1200
IMEP (bar)	3.9	4.1
Injection pressure (bar)	1600	1600
Intake temperature (°C)	90	70
BDC temperature (°C)	92	78
Intake pressure (kPa)	214	202
TDC motored temperature (K)	870	840
TDC motored density (kg/m^3)	22.9	22.5
Peak adiabatic flame temperature (K)	2256	2164
SOI (°ATDC)	−22.5	−0.5
Injection quantity (mg)	56	56
DOI (CAD)	7.75	7.75
O_2 concentration (vol%)	12.7	12.7

2.3. Radius of influence for collision probability

In the O'Rourke collision model [3], the gas phase cell is defined as the collision control volume and a collision can occur only if two parcels occupy the same cell. The probability of collision is estimated from the local number density of drops and the relative velocity between the drops using arguments similar to those in the kinetic theory of gases. Obviously, predictions with this model can show dependence on the size of the gas phase cell.

The present collision model based on the ROI (radius of influence) approach [15,16] uses a fixed collision radius of 2.0 mm around a parcel within which the potential collision partners are selected. The ROI is also used to define the spherical collision control volume around each parcel. This approach allows for collision calculations without the need for a separate collision mesh.

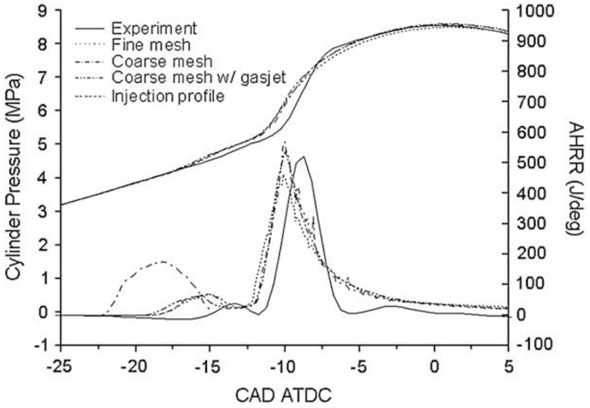

Fig. 4. Pressure trace and heat release of the early injection case (see Table 3).

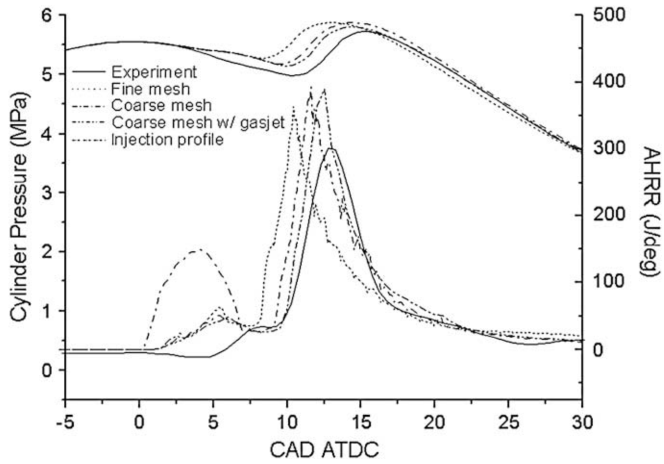

Fig. 5. Pressure trace and heat release of the late injection case (see Table 3).

If lp denotes the less populous parcel, mp denotes the more populous parcel and $D_{\mathrm{lp,mp}}$ is the distance between them, a collision is possible only if,

$$D_{\mathrm{lp,mp}} \leq R_{\max} \tag{14}$$

where $R_{\max} = \max(R_{\mathrm{lp}}, R_{\mathrm{mp}})$, and R is the effective parcel radius [15,16].

The collision frequency of one drop in the less populous parcel with all the drops in the more populous parcel is given by

$$\lambda = \frac{n_{\mathrm{mp}}\pi\left(r_{\mathrm{lp}} + r_{\mathrm{mp}}\right)^2 U}{V_{\mathrm{col}}} \tag{15}$$

where n is the number of drops in the parcel, r is the drop radius (assumed to be the same for all drops in a parcel), U is the relative velocity between the drops and V_{col} is the spherical control volume given by

$$V_{\mathrm{col}} = \frac{4\pi\left(R_{\mathrm{lp}} + R_{\mathrm{mp}}\right)^3}{3} \tag{16}$$

The probability of not having a collision in a time-step dt is given by

$$P_{\mathrm{nocol}} = \mathrm{e}^{-\lambda\,\mathrm{d}t} \tag{17}$$

Following O'Rourke [3], a uniform random number X is chosen in the interval (0,1) and collision occurs only if,

$$X > P_{\mathrm{nocol}} \tag{18}$$

The potential collision outcomes considered in the present study consisted of coalescence and grazing separations, as in the standard KIVA code.

2.4. *Ignition and main combustion*

A skeletal reaction mechanism for n-heptane [20] with 30 species and 65 reactions was used to simulate the diesel fuel chemistry. The mechanism was validated using constant volume ignition delay data and engine combustion experiments. The physical properties of tetradecane (c14h30) were used to model the fuel properties for the diesel injection, breakup and evaporation processes.

The CHEMKIN chemistry solver [21] was integrated into KIVA-3V to solve the n-heptane reaction mechanism. The convective and diffusive transport is modeled using the RNG k–ε turbulence model, and sub-grid scale turbulence-chemistry interaction is not considered (i.e., the mixture is assumed to be homogeneous within each computational cell). This approach has been found to provide accurate results also for cases with relatively long ignition delay times and sufficient fuel–air mixing, as in the present study.

The interpreter of CHEMKIN is first executed to generate a binary linking file that contains all the reactions and species information as an input to KIVA. An interface program was developed such that CHEMKIN is used as the chemistry subroutine in KIVA. Species and thermodynamic conditions are passed to the CHEMKIN solver, and the reaction mechanism is then solved for every computational cell at each time-step.

The reactive mixture in each computational cell is treated as a closed system in which the rate of change of mass fraction, Y_k, for each individual species is given as

$$\frac{\mathrm{d}Y_k}{\mathrm{d}t} = \frac{\dot{\omega}_k W_k}{\rho} \tag{19}$$

where ρ is the gas density, $\dot{\omega}_k$ is the volumetric production rate and W_k is the molecular weight of species k. By using the ideal gas mixture assumption, the energy equation can be written as (under constant volume conditions)

$$c_v\frac{\mathrm{d}T}{\mathrm{d}t} + \frac{1}{\rho}\sum_{k=1}^{K} e_k\dot{\omega}_k W_k = 0 \tag{20}$$

where c_v is the mean specific heat of the mixture, T is the cell temperature and e_k is the internal energy of species k. This formulation is consistent with the KIVA formulation that solves the internal energy equation, since the volume of the computational cell is not updated until the final rezoning phase.

2.5. *NO_x and soot models*

In the present KIVA-CHEMKIN code NO_x emissions are simulated by a reduced NO mechanism that was derived from the GRI NO mechanism of Smith et al. [22]. Consequently, four additional species (N, NO, NO_2, N_2O) and nine reactions are added to the n-heptane chemistry mechanism [23]:

(1) $N + NO \Leftrightarrow N_2 + O$
(2) $N + O_2 \Leftrightarrow NO + O$
(3) $N_2O + O \Leftrightarrow 2NO$
(4) $N_2O + OH \Leftrightarrow N_2 + HO_2$
(5) $N_2O + M \Leftrightarrow N_2 + O + M$
(6) $HO_2 + NO \Leftrightarrow NO_2 + OH$
(7) $NO + O + M \Leftrightarrow NO_2 + M$
(8) $NO_2 + O \Leftrightarrow NO + O_2$
(9) $NO_2 + H \Leftrightarrow NO + OH$

The reactions account only for thermal NO_x formation; prompt NO_x chemistry was not modeled since lean combustion conditions were considered. Three of the nine reactions are the extended Zeldovich reactions, and the rest account for thermal NO_x formation through NO_2 and N_2O reactions' pathways. The NO_2 and N_2O reactions were considered due to the fact that the LTC favors the formation of these two NO_x species over NO formation [24].

Soot emissions were predicted by a phenomenological soot model that uses competing formation and oxidation rates. The formation rate $\mathrm{d}m_{\mathrm{s,f}}/\mathrm{d}t$ is described by the Hiroyasu soot formation

Table 4
Comparison of liquid and vapor fuel distributions for the early injection case.

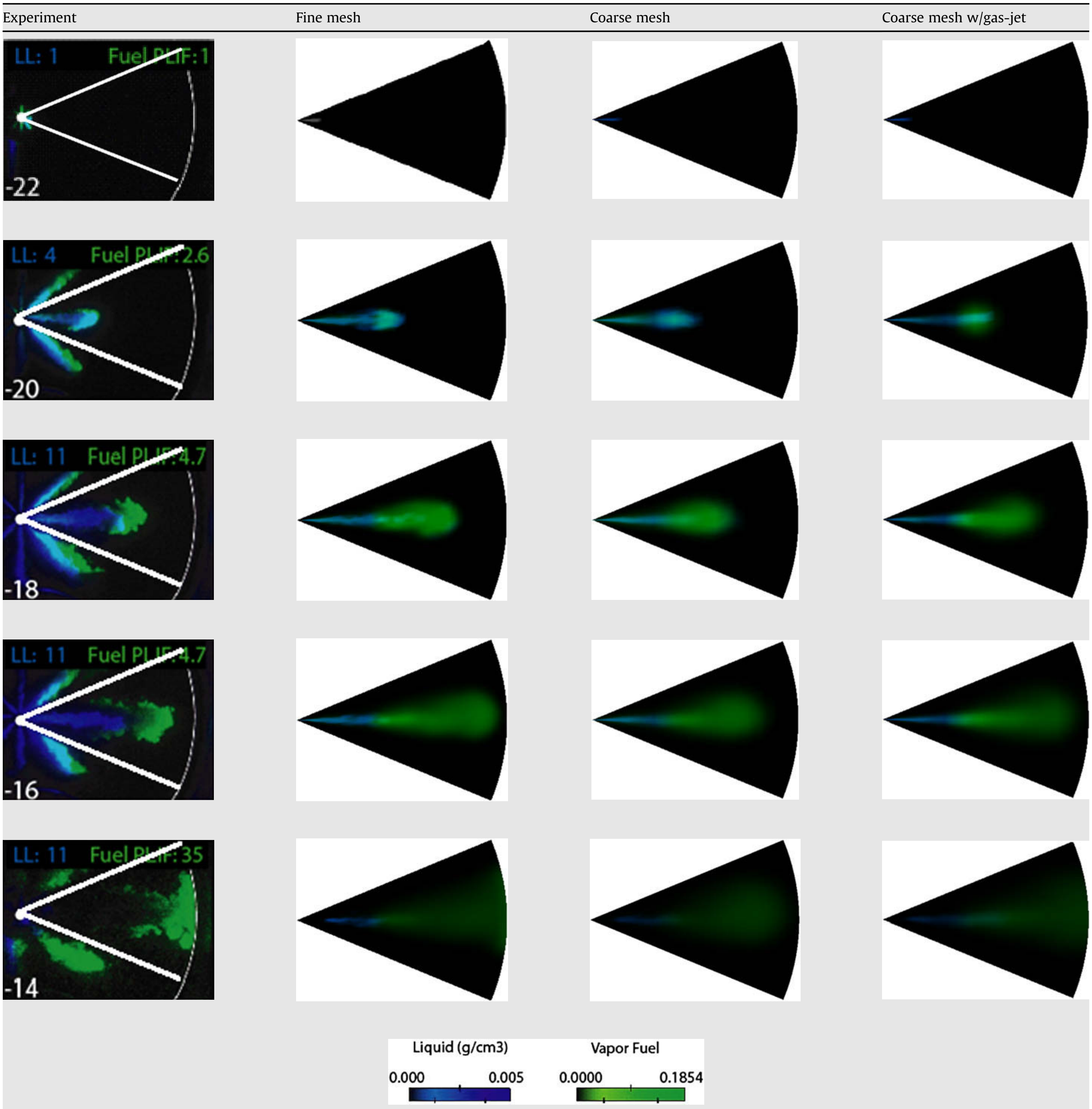

model [25] while the oxidation rate $\mathrm{d}m_{s,ox}/\mathrm{d}t$ is predicted by the Nagle–Strickland–Constable oxidation model [26] as follows:

$$\frac{\mathrm{d}m_s}{\mathrm{d}t} = \frac{\mathrm{d}m_{s,f}}{\mathrm{d}t} - \frac{\mathrm{d}m_{s,ox}}{\mathrm{d}t} \tag{21}$$

$$\frac{\mathrm{d}m_{s,f}}{\mathrm{d}t} = A_f m_{f,v} p^{0.5} \exp\left[-\frac{E_{s,f}}{RT}\right] \tag{22}$$

$$\frac{\mathrm{d}m_{s,ox}}{\mathrm{d}t} = \frac{6\mathrm{MW_C}}{\rho_s D_s} m_s R_{tot} \tag{23}$$

where A_f is the pre-exponential constant, $m_{f,v}$ is the mass of vaporized fuel, $E_{s,f}$ is the activation energy, $\mathrm{MW_C}$ is the carbon molecular weight, ρ_s is the soot density, D_s is a characteristic soot particle diameter, and R_{tot} denotes the total soot oxidation. In the model, acetylene (C_2H_2) is used as the soot formation species instead of "fuel", since it is an important precursor species. The soot

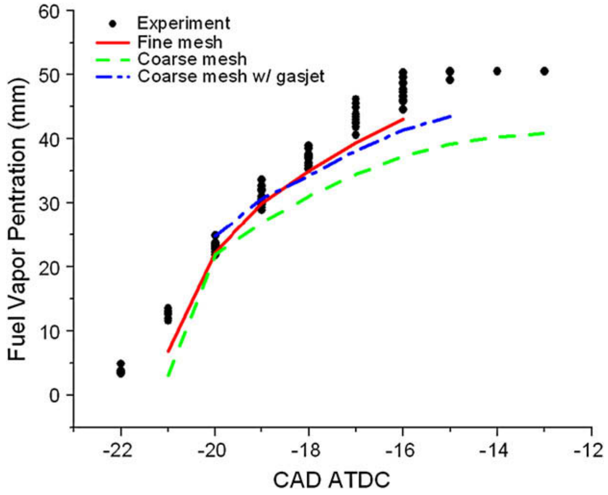

Fig. 6. Measured [18] and predicted vapor penetration distance of the early injection case.

model is not part of the reaction mechanism, and the soot formation/oxidation was calculated following the major combustion and NO chemistry calculations. The present soot model has been validated and predicts the sooting tendency of diesel sprays under constant volume conditions very well [23].

3. Experimental setup and diagnostics

3.1. Experiment setup

A single-cylinder, direct injection (DI), 4-stroke diesel engine based on a Cummins N-series production engine was used in this investigation. A schematic of the engine is shown in Fig. 2, and the specifications of the engine and the fuel injector are summarized in Table 1. The properties of the Phillips petroleum ultra-low sulfur 2007 emissions certification number 2 Diesel fuel used in the current study are shown in Table 2 [18]. To provide optical access, the engine is equipped with an extended piston and a flat piston-crown window. A window replaces one of the two exhaust valves in the cylinder head to provide imaging access to the squish region, although it was not used for the data modeled in the current study. A complete description of the engine is available in Espey and Dec [27], Dec [28], and Musculus [29].

3.2. Engine performance and diagnostics

The measured cylinder pressure was recorded at half-CAD increments [18]. Prior to calculating the apparent heat release rate (AHRR), the experimental pressure data were smoothed in the frequency domain using a low-pass filter with a Gaussian roll-off function having a transmission of 100% from 0 to 800 Hz and dropping to 1% at 3360 Hz. These cut-off frequencies were selected to remove acoustic ringing in the cylinder pressure data, while retaining the general features of the AHRR [18,29].

3.3. Laser diagnostics

3.3.1. Liquid–fuel penetration (LL)

A laser sheet from a 532-nm, 10-Hz pulsed Nd:YAG laser beam illuminated the liquid-phase fuel so that the spray penetration, or liquid length could be imaged via Mie scattering of the liquid–fuel droplets [18]. Depending on the complementary diagnostics, one of the two UV-sensitive, gated and intensified CCD cameras captured the elastically scattered light (see Fig. 2). A 532-nm center wavelength band-pass filter placed in front of a Nikon 50-mm f/1.2, glass camera lens set to f/11, isolated the elastically scattered laser light from other sources of emission (e.g., combustion luminosity, laser-heated soot, etc.). Additionally, a neutral density filter necessarily reduced the collected intensity by about three orders of magnitude for the intensified camera [18]. The camera electronic gate width was set to about 100 ns, and a more detailed description can be found in Espey and Dec [27].

3.3.2. OH planar laser induced fluorescence (OH-PLIF)

OH fluorescence was excited by pumping the overlapping Q1(9) and Q2(8) lines of the (1,0) band of the A ↔ X transition near 284 nm (vacuum wavelength). A UV-sensitive, gated, intensified camera (Camera 2 in Fig. 2) imaged the resulting fluorescence emission from multiple rotational transitions in both the (0,0) and (1,1) vibrational bands in the 308–320-nm range. A set of three filters helped to isolate the OH fluorescence and rejected elastic scatter: (1) a 312-nm center wavelength unblocked filter with a 16-nm full width at half maximum isolated the OH fluorescence, (2) a short-wave-pass filter with a cut-off near 358 nm rejected red-shifted fluorescence and other interference not blocked by the 312-nm filter, and (3) a 2 mm thick WG 305 long-wave-pass colored-glass filter helped to remove elastically scattered laser light [18]. The images were acquired using a camera gate width set to about 120 ns. More details, including the filter selection criteria, can be found in Dec and Coy [30].

Interference from fluorescence of other species, particularly including formaldehyde, polycyclic aromatic hydrocarbons (PAHs), and fuel species, as well as other emission sources (e.g., soot incandescence) may occur within the same band as the OH fluorescence (308–320 nm). OH displays a unique, well-defined fine-scale ro-vibrational structure in its fluorescence excitation spectrum. As a result, the OH fluorescence decreases drastically as the laser wavelength is tuned off of any of the narrow excitation lines. Therefore, to identify the extent and spatial location of the interference, the OH-PLIF images were taken at two different wavelengths: online, near 284 nm, and offline, near 283.9 nm [18]. A strong contrast between online and offline images indicates that the fluorescence is dominated by OH, while weaker contrast indicates that other sources contribute to the signal.

3.3.3. Planar laser induced fluorescence of fuel (Fuel-PLIF)

A typical multi-component number 2 diesel fuel was used in the experiments [18], which contains a significant fraction of aromatic hydrocarbons that show strong fluorescence with UV excitation. The fluorescence excitation is broadband (i.e., it does not display any fine-scale structure), and the emission is also broadband and overlaps with the OH fluorescence collection band [31]. On one hand this can create an undesirable source of interference for the OH-PLIF diagnostic, but it can also provide useful information about the mixing and penetration of the vapor-phase fuel. In contrast to the OH fluorescence verification described above (online/offline wavelength tuning), fuel fluorescence shows no dependence on small changes in laser excitation wavelength. Hydrocarbon synthesis reactions during combustion can also create other fluorescing species that may display broadband excitation/emission features. However, these synthesis reactions are not significant in the low temperature pre-ignition mixtures, so the primary broadband fluorescing species are expected to be fuel components [18]. Therefore, prior to the start of high-temperature combustion, UV fluorescence emission that does not display a strong online/offline contrast is interpreted as fuel fluorescence. Fuel fluorescence can arise from excitation of both liquid- and vapor-fuel, and the local fluorescence signal also depends strongly on the attenuation of the

Table 5
Comparison of liquid- and vapor-fuel for the late injection case.

Experiment	Fine mesh	Coarse mesh	Coarse mesh w/gas-jet
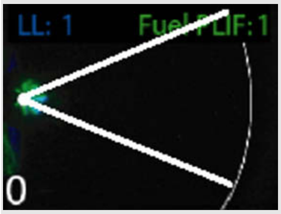	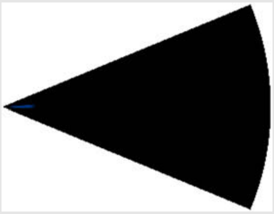	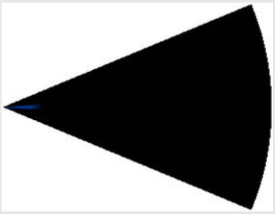	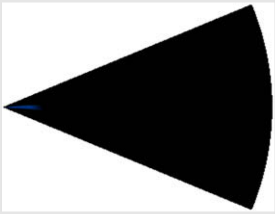
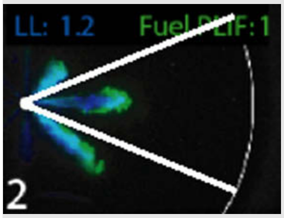	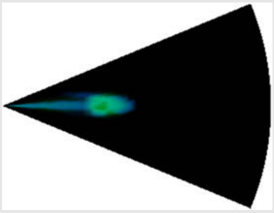	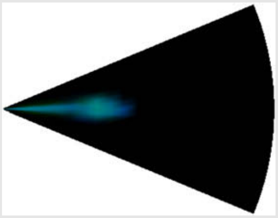	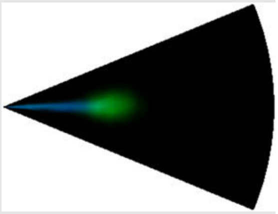
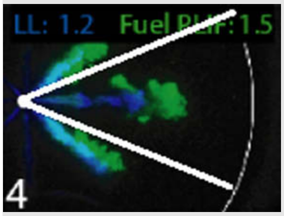	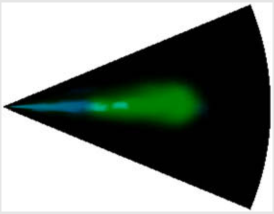	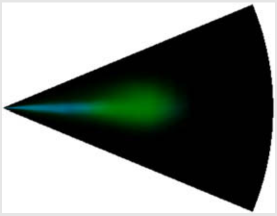	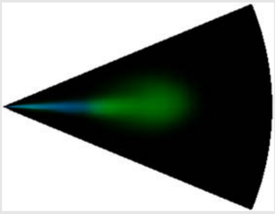
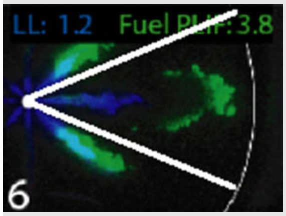	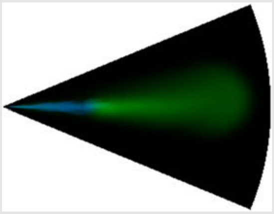	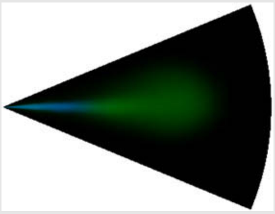	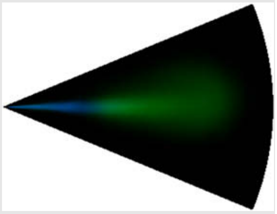
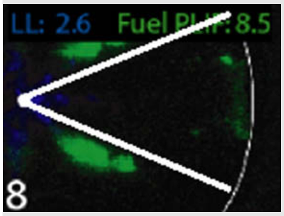	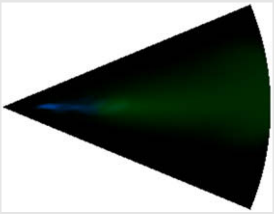	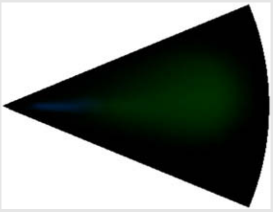	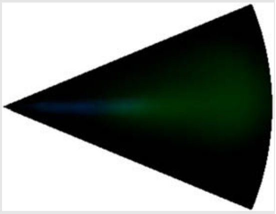
			

laser sheet in downstream regions of the jet. Fuel fluorescence images therefore must be interpreted with care, but interpretation is aided by comparison with liquid–fuel elastic-scattering images. Fuel fluorescence images were acquired with the same UV-sensitive, gated, intensified camera as used for OH-PLIF (Camera 2 in Fig. 2), with the electronic gate width set to 120 ns and equipped with the same set of three filters as described in the OH-PLIF section [18].

3.3.4. Planar laser induced incandescence of soot (Soot-PLII)

In the study of Singh [18] the soot LII was excited with the same 532-nm, 10-Hz pulsed, laser sheet used for the liquid fuel penetration. Although the pulse energy (35 mJ) was lower than that used in previous studies in this engine (e.g., 120 mJ by Dec and Kelly-Zion [32]), the lower energy was found to be sufficient to illuminate the soot while avoiding excessive interference from

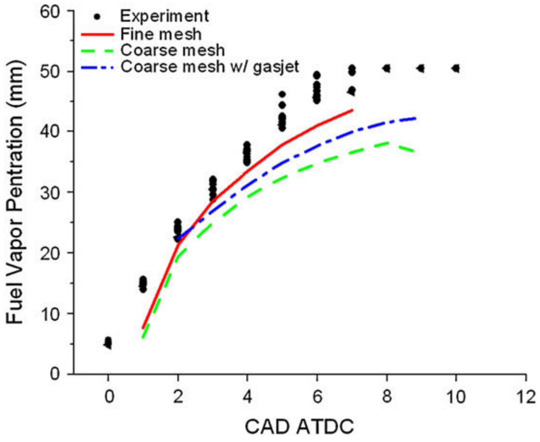

Fig. 7. Measured [18] and predicted vapor penetration for the late injection cases.

"flare" where the beam struck the cylinder head. A UV-sensitive, gated, intensified, camera with a Nikon 50-mm, f/1.2, glass lens (Camera 1 in Fig. 2), with gate width set to about 100 ns, acquired the LII images. A short-wave-pass filter with a cut-off near 450-nm helped to reject naturally-occurring soot luminosity, and a 532-nm notch filter rejected elastically scattered laser light [18].

4. Results and discussion

4.1. Computational grid and initial conditions

4.1.1. Computational grid

The piston geometry and two different computational grid densities (i.e., a fine and a coarse grid) used in the simulations are shown in Fig. 3. The diesel injector had eight equally spaced nozzle holes, so the combustion chamber was represented by a 45° sector mesh with assumed periodic boundary conditions. All major geometric dimensions of the combustion chamber, including the cylinder bore, stroke, bowl dimensions and squish height were replicated in the computational grids.

Additional grids were introduced in the crevice region to account for the additional volume occupied by the ring land, valve, and optical window crevices. In this way, the geometric compression ratio in the model was maintained to be the same as the experimental engine. The grids were created using the standard KIVA-3V pre-processor. The fine mesh was composed of 76,514 computational cells at bottom dead center (BDC) with approximately $1.2 \times 1.2 \times 1.2$ mm cell sizes near the piston bowl wall. The coarse mesh was composed of 19,386 computational cells at BDC with approximately $2.4 \times 2.4 \times 2.4$ mm cell sizes near the piston bowl wall.

4.1.2. Initial conditions

The computations were started from intake valve closure (IVC $= -165$ ATDC) with an assumed uniform mixture distribution in the cylinder. The swirl was initialized based on the so-called Wheel Flow velocity profile [33]. For low-swirl heavy-duty DI engines, the turbulent kinetic energy near TDC is not very sensitive to the initialization of the turbulence quantities at IVC [34]. A low value of turbulent kinetic energy ($<1\%$ of mean piston speed) and a small length scale (10% of cylinder bore) were assumed at IVC to initialize the turbulent flow field. The pressure at IVC was initialized based on the experimental pressure trace, and the IVC temperature was calculated assuming isentropic compression from BDC to IVC. The injection rate-shape was taken from experimental data, acquired using a momentum-based rate-of-injection meter [35].

4.2. Low temperature injection strategies

As emissions' regulations for diesel engines are becoming more stringent worldwide, recent diesel combustion research is focusing on low temperature combustion (LTC) [36–41]. LTC achieves a simultaneous reduction of nitrogen oxides (NO_x) and particulate matter (PM) emissions by suppressing combustion temperatures and by premixing fuel with the in-cylinder charge prior to ignition. In one class of LTC strategies, which includes homogeneous charge compression ignition (HCCI), fuel is mixed with the intake charge prior to compression [39–41]. Alternatively, fuel may be mixed with the air charge after compression, using a relatively late fuel injection with a large amount of exhaust gas recirculation and typically high swirl (e.g., Nissan's "MK" combustion concept [36,37]).

In this study two different injection strategies were selected for the low temperature operating conditions: early injection and late injection, as shown in Table 3. The late injection condition is similar to the so-called MK combustion operating condition suggested by the Nissan group [36,37]. However, there are some differences. The swirl ratio (0.5) is not as high as that in typical MK combustion conditions (3 or more). Also, there is a smaller ignition dwell (the period between end of injection and start of combustion) than for previous MK combustion implementations. In spite of these differences, many in-cylinder processes are still expected to be similar to the MK combustion reported by Kimura et al. [36,37].

4.3. Model validation

4.3.1. Cylinder pressure and apparent heat release rate (AHHR)

For the purposes of comparison, both the experimental [18] and the present computational AHRRs were calculated from the cylinder pressure using the air standard cycle, assuming no heat transfer to the walls [42]. For early injection, the fuel is injected early at $-22.5°$ ATDC, as shown in Fig. 4. To realize the LTC conditions, the intake mixture was diluted with nitrogen such that the oxygen concentration of the intake stream was only 12.7% by volume. Heat release from the cool flame (CF) chemistry is first observed in the experiments at $-15°$ ATDC after an ignition delay (ID) of 7 CAD. After a period of very low heat release rate, the second stage combustion (SSC) starts at $-12°$ ATDC. The start of SSC timing and the resulting rate-of-heat release are fairly well predicted by all the models. There are no obvious differences of the cylinder pressure and apparent heat release curves between fine mesh, coarse mesh with and without use of the gas-jet model for the early injection case.

Fig. 5 shows cylinder pressure and AHRR for the low temperature, late injection condition. The fuel injection begins at $-0.5°$ ATDC. Significant heat release from CF reactions is observed in the experiments after an ID of about 6.25 CAD. The CF ID is underpredicted by the present KIVA-CHEMKIN model. But the results obtained with the coarse mesh with the gas-jet model show better agreement with the experiments than the results of the coarse mesh without the gas-jet model due to improvement of the prediction of the spray droplet–gas relative velocity and the updated collision model.

4.3.2. Liquid, vapor fuel distributions and penetrations

Table 4 shows a comparison of the experimental laser Mie scattering (LMS) from the liquid fuel droplets (blue) and the broadband planar laser induced fluorescence (BB-PLIF) (green) images (left column) with the model-predicted liquid fuel density and vapor fuel mass fraction distributions (three columns on right)

Table 6
Comparison of soot and OH distributions for the early injection case.

Experiment	Fine mesh	Coarse mesh	Coarse mesh w/gas-jet
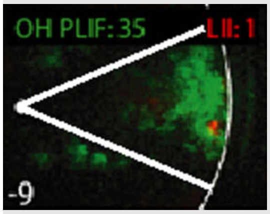	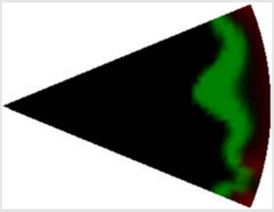	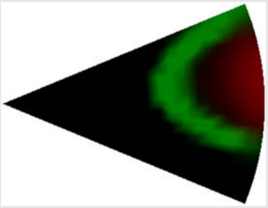	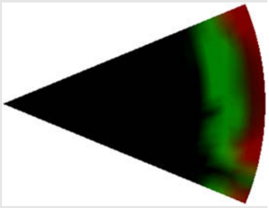
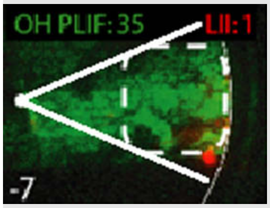	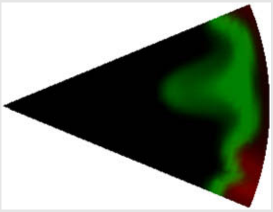	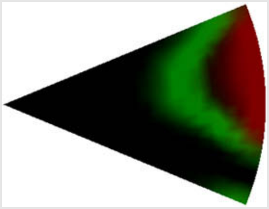	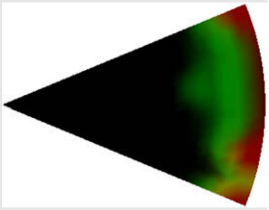
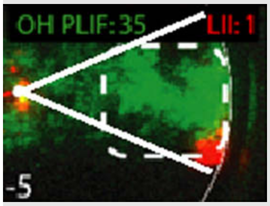	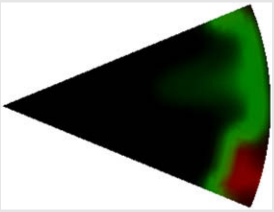	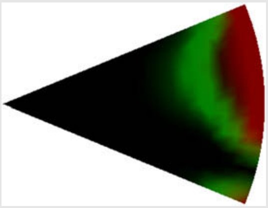	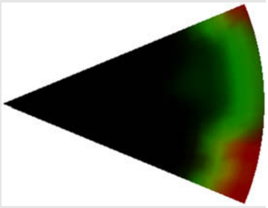
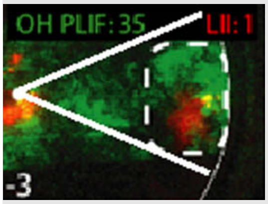	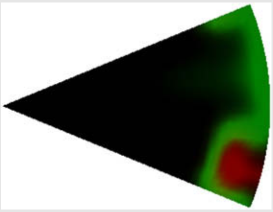	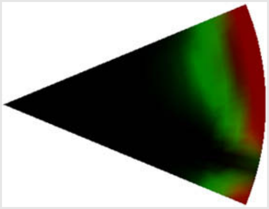	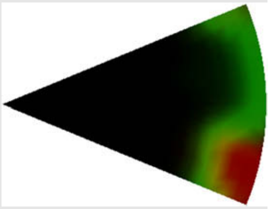
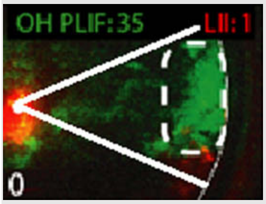	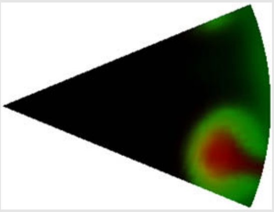	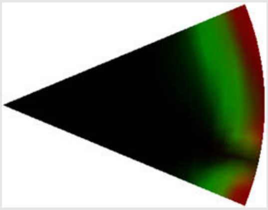	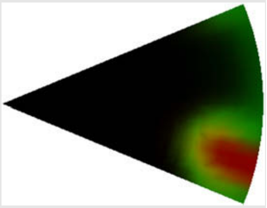
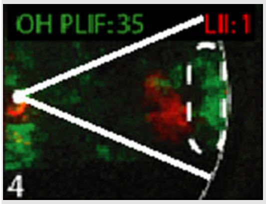	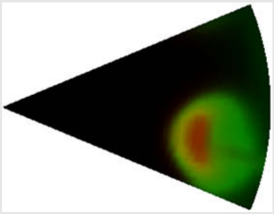	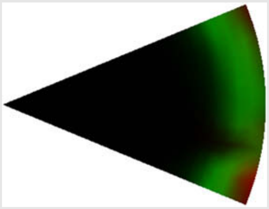	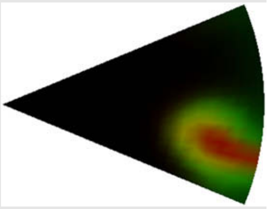

Table 7
Comparison of soot and OH distributions of the late injection case.

Experiment	Fine mesh	Coarse mesh	Coarse mesh w/gas-jet
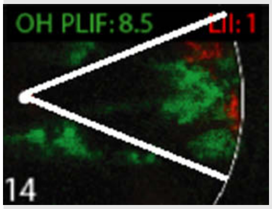	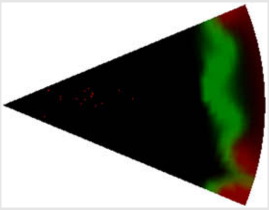	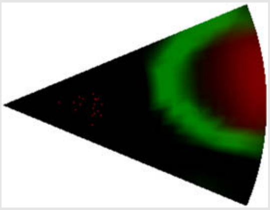	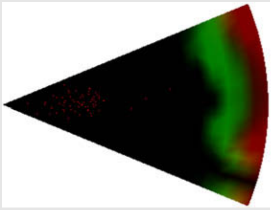
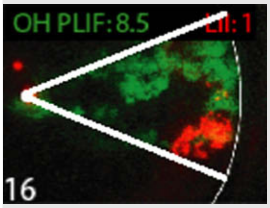	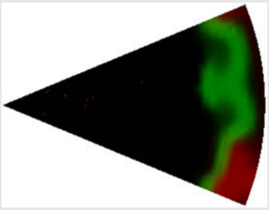	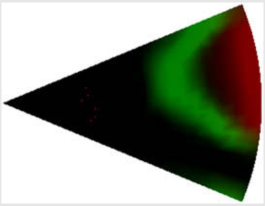	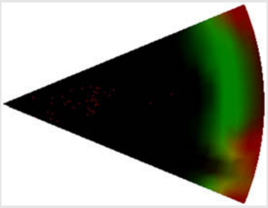
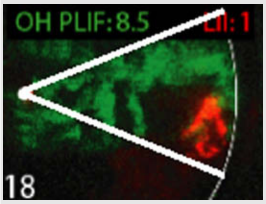	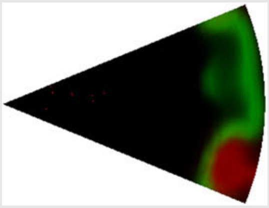	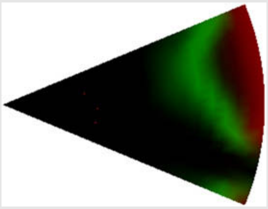	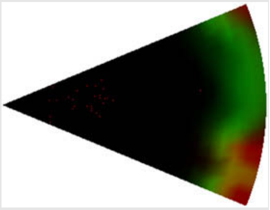
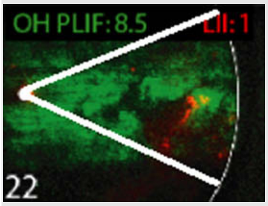	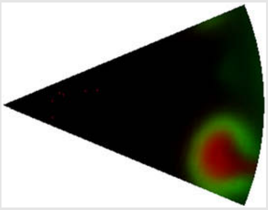	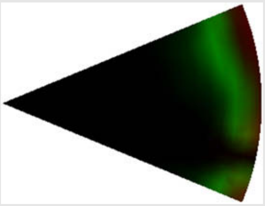	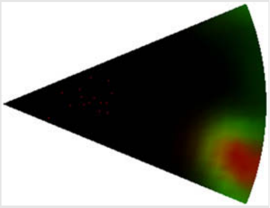

for the early injection condition. The field of view does not encompass the entire combustion chamber, but focuses on one of the eight jets at the 3 o'clock position from the camera's perspective. The white curve on the right of each experimental image represents the inner surface of the piston bowl, which is about 49 mm away from the injector tip, which is indicated by a white dot on the left side of each image [18]. The number in the bottom-left corner of each experimental image is the crank angle at which the image was taken. The fuel vapor penetrations are compared, as shown in Fig. 6.

From the figures, it can be seen that the fine mesh results show good agreement with the experiments in terms of the predicted extents of the liquid–vapor distributions and the vapor penetration. But the coarse mesh results have a shorter vapor penetration than the fine mesh case, as shown in Fig. 6. This is due to errors in predicting the droplet–gas relative velocity and errors in describing droplet–droplet collision and coalescence processes. When the gas-jet and ROI models are considered, the vapor penetration of the coarse mesh can be improved to the same level as the fine mesh results, as shown in Table 4 and Fig. 6.

Similarly, Table 5 presents a comparison of the experimental LMS from the liquid fuel droplets (blue) and the BB-PLIF (green) images (left column) with the model predicted liquid–vapor fuel distributions (three columns on right) for the late injection condition. The fuel vapor penetrations are compared in Fig. 7. A similar improvement for the late injection case as that seen for the early injection case is seem with the coarse mesh when the gas-jet and ROI models are used.

4.3.3. *In-cylinder OH and soot distributions*

For the early injection case soot was present in the experiments in tiny isolated pockets at somewhat random locations [18]. An image most representative of the ensemble-averaged behavior at each crank angle from a set of 20 images from different engine cycles was chosen for presentation. These images are presented in Table 6, which shows simultaneous images of OH-PLIF (green) and soot LII (red) from the experiments (left column), along with the model predicted OH (green) and soot (red) mass fractions (right three columns), all in a plane along the jet axis. Comparison of the online and offline OH-PLIF images shows strong contrast only in the downstream regions (white dot circle line) near the piston bowl wall, indicating the presence of the highly-oxidizing radical OH, and thus significant SSC chemistry. In the upstream regions, however, the online and offline OH-PLIF signals were of similar strength, so other broadband fluorescence sources contribute to the majority of the emission (i.e., BB-PLIF) [18].

Starting at the beginning of the sequence in Table 6 at −9° ATDC, the fine mesh model predicts soot near the piston bowl wall surrounded by a ribbon-like OH radical distribution. This captures the main soot formation position seen at the right-bottom location near the bowl wall and the downstream OH formation seen in the experiments in Table 6. However, due to the shorter vapor fuel penetration compared to the fine mesh model, the simulation results of the coarse mesh model show the soot being formed near the right-top location near the bowl wall and the OH distribution spherically surrounds the soot, which is in disagreement with the results of the experiments and fine mesh model. However, if the gas-jet and ROI models are employed, the soot and OH distributions predicted with the coarse mesh can be improved to the same level as that of the fine mesh, as shown in Table 6.

For the late injection case Table 7 gives the corresponding comparisons of the model-predicted OH (green) and soot (red) mass fractions with simultaneous experimental images of OH-PLIF (green) and soot-LII (red), in a plane along the jet axis. The experimentally observed OH-PLIF distributions are similar to the above discussed early injection LTC condition [18]. The fluorescence from OH radicals, as indicated by strong online/offline contrast, is dominant only in the downstream region in the experimental images. The fluorescence in the upstream region is insensitive to laser wavelength and is therefore mostly from broadband sources, likely unburned fuel and combustion intermediates [18]. The experimentally observed soot-LII distributions are also somewhat similar to the early injection LTC condition. The cycle-to-cycle variations of the location of bright spots of LII are lower, however, and the soot is still found mostly in the jet's head vortex region, as is evident from the 16 and 18 ATDC images in the left column of Table 7.

The fine mesh model-predicted OH and soot distributions reveal a high concentration ribbon-like OH structure surrounding the soot formation region, and are very similar to the early injection LTC condition. Similarly, due to the shorter vapor fuel penetration compared to the fine mesh model, the coarse mesh model simulations are very different from the results of the experiments and the fine mesh model. However, the soot and OH distributions of the coarse mesh with gas-jet and ROI models are significantly improved, as shown in Table 7.

5. Conclusions

A new spray model has been formulated and tested that assumes that the gas velocity in the unresolved regions near the injector nozzle can be modeled using a gas-jet theory, and the collision probability for droplets in the gas phase computational cells can be estimated using a radius of influence (ROI) of collision methodology. The model predicts more accurately the relative velocity between the droplets and the gas, and also reduces the dependence of the results on the size of the gas phase cell. In the model the gas-jet submodel is only applied in the under-resolved, near-field region up to a distance of twice the jet breakup length and the ROI is fixed with a collision radius of 2.0 mm.

The improved spray model was applied to simulate spray processes in early and late injection low temperature diesel combustion regimes with fine and coarse meshes. Compared with the results of a coarse mesh without using the gas-jet and ROI models, the new spray model is shown to provide predictions that agree well with experimental results and with simulation results obtained with the fine mesh in terms of significantly reduced mesh sensitivities.

Acknowledgement

The authors gratefully acknowledge support for this work from General Motors Research & Development and DOE LTC Consortium project DE-FC26-06NT42628.

References

[1] N. Abani, A. Munnannur, R.D. Reitz, Reduction in numerical parameter dependencies in diesel spray models, ASME Journal of Engineering for Gas Turbine and Power 130 (2008) 032810.

[2] J. Abraham, What is adequate resolution in the numerical computation of transient jets, SAE paper 970051, 1997.

[3] P.J. O'Rourke, F.V. Bracco, Modeling drop interactions in thick sprays and a comparison with experiments, in: Stratified Charge Automotive Engines, I. Mech. E. Conference Publications 1980–9, 1980, pp. 101–116.

[4] S. Post, V. Iyer, J. Abraham, A study of the near-field entrainment in gas jets and sprays under diesel conditions, ASME Journals of Fluids Engineering 122 (2000) 385–395.

[5] R. Aneja, J. Abraham, How far does the liquid penetrate in diesel engine: computed results vs. measurements? Combustion Science and Technology 138 (1–6) (1998) 233–255.

[6] P. Beard, J.M. Duclos, C. Habchi, G. Bruneaux, K. Mokaddem, T.A. Baritaud, Extension of Lagrangian–Eulerian spray modeling: application to high-pressure evaporating diesel sprays, SAE technical paper 2000-01-1893, 2000.

[7] D.P. Schmidt, C.J. Rutland, A new droplet collision algorithm, Journal of Computational Physics 164 (2000) 62–80.

[8] D.P. Schmidt, C.J. Rutland, Reducing grid dependency in droplet collision modeling, ASME Journal of Engineering for Gas Turbines and Power 126 (2004) 227–233.

[9] A.M. Lippert, S. Chang, S. Are, D.P. Schmidt, Mesh independence and adaptive mech refinement for advanced engine spray simulations, SAE technical paper 2005-01-0207, 2005.

[10] J.C. Beale, R.D. Reitz, Atomization and Sprays 9 (1999) 623–650.

[11] J. Abraham, Entrainment characteristics of transient jets, Numerical Heat Transfer, Part-A 30 (1996) 347–364.

[12] H. Schlichting, Boundary Layer Theory, McGraw-Hill, New York, 1976.

[13] N. Abani, S. Kokjohn, S.W. Park, M. Bergin, A. Munnannur, Y. Sun, W. Ning, R.D. Reitz, An improved spray model for reducing numerical parameter dependencies in diesel engine CFD simulations, SAE technical paper 2008-01-0970, 2008.

[14] N. Abani, R.D. Reitz, Unsteady turbulent round jets and vortex motion, Physics of Fluids 19 (2007) 125102.

[15] A. Munnannur, R.D. Reitz, A comprehensive collision model for engine spray computations, in: Proceedings of ILASS Americas 2008, Orlando, FL, USA, 2008.

[16] A. Munnannur, R.D. Reitz, Droplet collision modeling in multi-dimensional engine spray computations, Ph.D. thesis, University of Wisconsin–Madison, 2007.

[17] A.A. Amsden, KIVA-3V: a block structured KIVA program for engines with vertical or canted valves, Technical report no. LA-13313-MS, Los Alamos National Laboratory, July 1997.

[18] S. Singh, Experimental investigation of multi-mode diesel engine combustion and validation of advanced combustion models, Ph.D. thesis, University of Wisconsin–Madison, 2006.

[19] P. Beard, O. Colin, M. Miche, Improved modeling of DI diesel engines using sub-grid descriptions of spray and combustion, SAE technical paper 2003-01-0008, 2003.

[20] A. Patel, R.D. Reitz, Development and validation of a reduced reaction mechanism for HCCI engine simulations, SAE technical paper 2004-01-0558, 2004.

[21] R.J. Kee, J.F. Gracer, J.A. Miller, E. Meeks, M.D. Smooke, Premix: a fortran code for modeling steady one-dimensional premixed flames, in: Reaction Design, California, USA, 1998.

[22] G.P. Smith, D.M. Golden, M. Frenklach, N.W. Moriarty, B. Eiteneer, M. Goldenberg, C.T. Bowman, R.K. Hanson, S. Song, W.C. Gardiner Jr., V.V. Lissianski, Z. Qin, GRI-Mech 3.0.http://www.me.berkeley.edu/gri_mech/ (2005).

[23] S.C. Kong, Y. Sun, R.D. Reitz, Modeling diesel spray flame lift-off, sooting tendency and NO_x emissions using detailed chemistry with phenomenological soot model, ASME ICES (2005).

[24] S.R. Turns, An Introduction to Combustion, McGraw Hill, New York, 2000.

[25] H. Hiroyasu, T. Kadota, Models for combustion and formation of nitric oxide and soot in DI diesel engines, SAE technical paper 760129, SAE transactions 85, 1976.

[26] J. Nagle, R.F. Strickland-Constable, Oxidation of carbon between 1000–2000 °C, in: Proceedings of the Fifth Carbon Conference, vol. 1, Pergamon Press, 1962, p. 154.

[27] C. Espey, J.E. Dec, The effect of TDC temperature and density on the liquid-phase penetration in a D.I. diesel engine SAE technical paper 952456, SAE Transactions 104 (4) (1995) 1400–1414.

[28] J.E. Dec, A conceptual model of D.I. diesel combustion based on lased sheet imaging SAE technical paper 970873, SAE Transactions 106 (3) (1997) 1319–1348.

[29] M.P.B. Musculus, On the correlation between NO_x emissions and the diesel premixed burn SAE technical paper 2004-01-1401, SAE Transactions 113 (4) (2004).

[30] J.E. Dec, E.B. Coy, OH radical imaging in a DI diesel engine and the structure of early diffusion flame SAE technical paper 960831, SAE Transactions 105 (3) (1996) 1127–1148.

[31] M.P.B. Musculus, Multiple simultaneous optical diagnostic imaging of early-injection low-temperature combustion in a heavy-duty diesel engine, SAE technical paper 2006-01-0079, 2006.

[32] J.E. Dec, P.L.K. Zion, The effects of ignition timing and diluent addition on late-combustion soot burnout in a DI diesel engine based on simultaneous 2-D imaging of OH and soot, SAE technical paper 2000-01-0238, 2000.

[33] A.A. Amsden, T.D. Butler, P.J. O'Rourke, J.D. Ramshaw, Kiva-A comprehensive model for 2-D and 3-D simulations SAE technical paper 850554, SAE Transactions 94 (4) (1985).

[34] S.H. El Tahry, A numerical study on the effects of fluid motion at inlet-valve closure on subsequent fluid motion in a motored engine, SAE technical paper 820035, 1982.

[35] M.P.B. Musculus, Effects of the in-cylinder environment on diffusion flame lift-off in a DI diesel engine SAE technical paper 2003-01-0074, SAE Transactions 112 (3) (2003) 314–337.

[36] S. Kimura, O. Aoki, Y. Kitahara, E. Aiyoshizawa, Ultra-clean combustion technology combining a low-temperature and premixed combustion concept for meeting future emission standards, SAE paper 2001-01-0200, 2001.

[37] S. Kimura, O. Aoki, H. Ogawa, S. Muranaka, Y. Enomoto, New combustion concept for ultra-clean and high-efficiency small DI diesel engines SAE paper 1999-01-3681, SAE Transactions 108 (3) (1999) 2128–2137.

[38] K. Akihama, Y. Takatori, K. Inagaki, S. Sasaki, A.M. Dean, Mechanism of the smokeless rich diesel combustion by reducing temperature, SAE paper 2001-01-0655, 2001.

[39] B. Walter, B. Gatellier, Development of the high power NADI concept using dual mode diesel combustion to achieve zero NO_x and particulate emissions, SAE paper 2002-01-1744, 2002.

[40] A. Minato, T. Tanaka, T. Nishimura, Investigation of premixed lean diesel combustion with ultra high pressure injection, SAE paper 2005-01-0914, 2005.

[41] T. Kanda, T. Hakozaki, T. Uchimoto, J. Hatano, N. Kitayama, H. Sono, PCCI operation with early injection of conventional diesel fuel, SAE paper 2005-01-0378, 2005.

[42] J.B. Heywood, Internal Combustion Engine Fundamentals, McGraw-Hill, Inc., 1988.